Journal of Volcanology and Geothermal Research 298 (2015) 59–70

Contents lists available at ScienceDirect

Journal of Volcanology and Geothermal Research

journal homepage: www.elsevier.com/locate/jvolgeores

Coupling geophysical investigation with hydrothermal modeling to constrain the enthalpy classification of a potential geothermal resource

J.T. White [a,c,*], A. Karakhanian [d], C.B. Connor [c], L. Connor [c], J.D. Hughes [b], R. Malservisi [c], P. Wetmore [c]

[a] U.S. Geological Survey, Texas Water Science Center, 1505 Ferguson Lane, Austin, TX 78754, United States
[b] U.S. Geological Survey, Office of Groundwater, 12201 Sunrise Valley Dr., Reston, VA 20192, United States
[c] School of Geosciences, University of South Florida, 4202 East Fowler Ave., Tampa, FL 33620, United States
[d] Institute of Geological Sciences, National Academy of Science of Armenia, 24 Marshall Baghramian Avenue, 0019 Yerevan, Armenia

ARTICLE INFO

Article history:
Received 20 October 2014
Accepted 20 March 2015
Available online 14 April 2015

Keywords:
Geophysical inversion
Hydrothermal modeling
Armenia
Distributed volcanism
Karckar
Gravity

ABSTRACT

An appreciable challenge in volcanology and geothermal resource development is to understand the relationships between volcanic systems and low-enthalpy geothermal resources. The enthalpy of an undeveloped geothermal resource in the Karckar region of Armenia is investigated by coupling geophysical and hydrothermal modeling. The results of 3-dimensional inversion of gravity data provide key inputs into a hydrothermal circulation model of the system and associated hot springs, which is used to evaluate possible geothermal system configurations. Hydraulic and thermal properties are specified using maximum a priori estimates. Limited constraints provided by temperature data collected from an existing down-gradient borehole indicate that the geothermal system can most likely be classified as low-enthalpy and liquid dominated. We find the heat source for the system is likely cooling quartz monzonite intrusions in the shallow subsurface and that meteoric recharge in the pull-apart basin circulates to depth, rises along basin-bounding faults and discharges at the hot springs. While other combinations of subsurface properties and geothermal system configurations may fit the temperature distribution equally well, we demonstrate that the low-enthalpy system is reasonably explained based largely on interpretation of surface geophysical data and relatively simple models.

Published by Elsevier B.V.

1. Introduction

The enthalpy of a geothermal resource is an important factor in determining suitability for electrical power generation and ultimately, economic viability (Reed et al., 1983; Sanyal, 2005; Rezaie and Aghajani, 2013). While understanding the role and scale of volcanic and tectonic processes provides important system enthalpy information (Muffler, 1993), determining the enthalpy classification of an undeveloped resource typically involves installation of test borings into the geothermal target (Gupta and Roy, 2006). Depending on the depth to target, test borings can represent a high-risk investment. Recognition of this cost has led to the use of geophysical data collection and analysis to reduce the investment risk and guide locating and constructing test borings (Jennejohn, 2009). See for example Zaher et al. (2011) and Zaher et al. (2012). However, even with the addition of geophysical analysis, the enthalpy classification for a given geothermal system remains uncertain prior to installation of test borings.

Here we present a novel coupling of gravity inversion with hydrothermal modeling to investigate an undeveloped geothermal system in the Karckar region of Armenia (Fig. 1). The system is located along the Pambak–Sevan–Sunik fault, a major strike-slip fault system formed at the boundary between the Eurasian and Arabian plates (Philip et al., 2001). In the Karckar region, recent distributed volcanism is associated with the fault zone, especially along pull-apart basins formed by changes in the overall strike of the fault (Fig. 1).

This study focuses on the use of geophysical methods coupled with hydrothermal circulation modeling to investigate the Karckar geothermal system. We use the results from high-resolution 3-dimensional gravity inversion to define the basin geometry, which controls the depth of circulation in the hydrothermal model. In addition to the results of the gravity inversion, local and regional geologic and hydrological data are used to specify properties and boundary conditions for a numeric groundwater flow model that simulates advective and conductive heat transport. Two geothermal target configurations are evaluated, representing a low- and high-enthalpy system, respectively. Temperature data from an existing down-gradient borehole are used in sensitivity analysis to identify the most likely system configuration and resulting enthalpy.

2. Geological setting

Armenia is located near the apex of the collision between the Arabian and Eurasian plates (Fig. 1) (Dewey et al., 1986). The region is characterized by the extrusion tectonics of the Anatolian plate to the west and the Iranian block to the east. The complexity of the tectonic

* Corresponding author.
E-mail address: jwhite@usgs.gov (J.T. White).

http://dx.doi.org/10.1016/j.jvolgeores.2015.03.020
0377-0273/Published by Elsevier B.V.

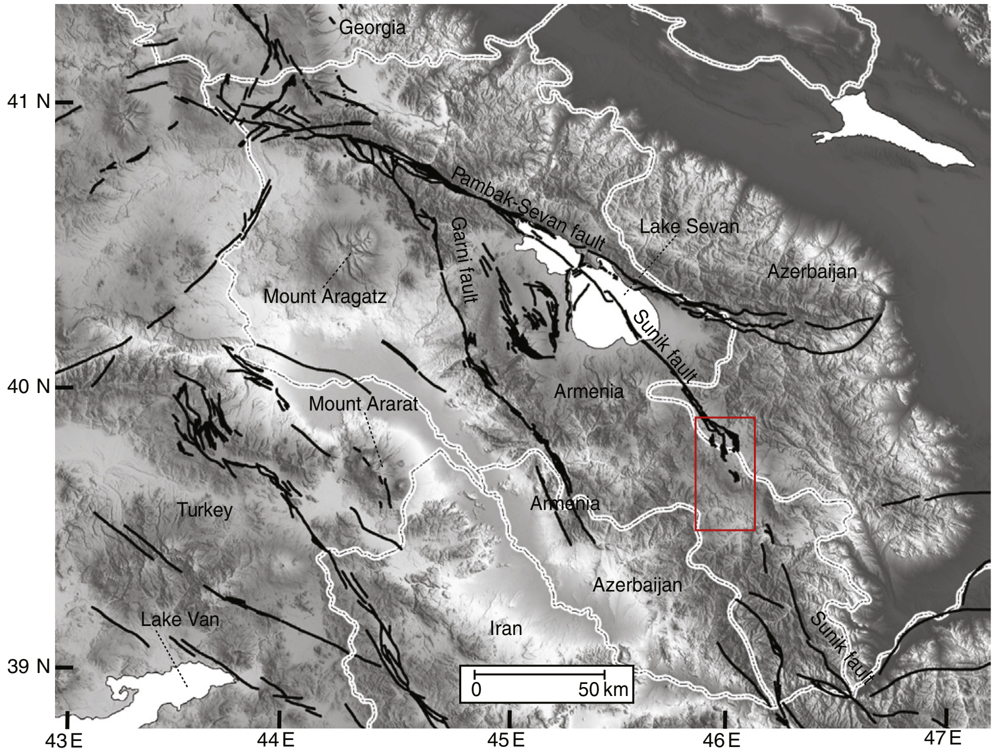

Fig. 1. Fault map of Armenia and surrounding region. Fault traces have been modified from Karakhanian et al. (2004). Red box shows the Karckar region and the approximate extent of Fig. 2. Digital elevation model obtained from the shuttle radar topography mission (CGIAR, 2008). Approximate scale is shown. (For interpretation of the references to color in this figure legend, the reader is referred to the web version of this article.)

setting is demonstrated by the contemporary presence of different tectonic stress regimes. Part of the convergence between Arabia and Eurasia is accommodated by east–west trending folds and thrust faults. Elsewhere, the east–west extension associated with the migration of the Iranian and Anatolian blocks is accommodated through block rotation and a complex network of strike-slip faults, which are generally dextral when trending to the northwest and sinistral when trending to the northeast (Philip et al., 1992, 2001; Rebai et al., 1993; Karakhanian et al., 2002, 2004; Copley and Jackson, 2006; Reilinger et al., 2006).

One of these dextral faults is the Pambak–Sevan–Sunik fault. The trace of the Pambak–Sevan–Sunik fault extends nearly 400 km from where it enters Armenia at the Iranian border to its northwestern terminus near the triple border between Armenia, Turkey and Georgia. The Pambak–Sevan–Sunik fault has been the subject of numerous studies since the M7.1 1988 Spitak earthquake (Philip et al., 1989, 1992, 2001; Trifonov et al., 1990, 1994; Karakhanian et al., 1997, 2002, 2004), which occurred on a splay of the Pambak–Sevan–Sunik fault in northern Armenia (Philip et al., 1992). The most recent of these studies (Philip et al., 2001; Karakhanian et al., 2004) have broken the Pambak–Sevan–Sunik fault into as many as six sections. However, for our purposes we discuss the Sunik section (Figs. 1 and 2).

The Sunik section, which traverses our study area, trends north to north–northwest, and is traceable from the Iranian border at the southern-most point in Armenia to the eastern shore at the center of Lake Sevan. The Sunik fault south of Lake Sevan is characterized by multiple small fault strands, and both dilational and contractional bends and step-overs (Karakhanian et al., 2002). One of the best expressed step-overs can be observed in the area of the Karckar volcanic field (Fig. 2). Here the Sunik fault, which trends northwest to both the north and south of the volcanic field, makes a 15 km right step (Karakhanian et al., 2002). Mapping by Karakhanian et al. (1997, 2002, 2004) identifies a relatively narrow (2–3 km wide) network of north-trending oblique (normal and dextral) slip faults bounding a shallow basin partially occupied by the distributed Karckar volcanic field, whose recent vents appear to be clustered in a north–south direction along the central part of the basin between the eastern and western network of faults. However, field observations and satellite imagery reveal evidence for a much larger distribution of volcanism than is depicted by the most recent volcanic events. While a minimum offset of 700 m can be inferred from faulted features like cinder cones, the total offset on the Sunik and the networks of basin-bounding faults is unknown in the Karckar region due to high volcanic production rates and the relatively slow slip rates.

3. Gravity

Gravity anomalies are created by different density distributions that create lateral discontinuities within the earth's crust. For example, gravity anomalies are frequently associated with faults; faults may juxtapose rocks of different densities and therefore create a change in the gradient of the gravity field. Relative gravity is measured at point locations where both the relative change in gravity and the precise location of the measurement (i.e., cm to mm accuracy in both the horizontal and vertical directions) are recorded (Sheriff, 1973).

This study is based on a high-resolution, ground-based, gravity survey, collected during the fall of 2011 within a narrow pull-apart basin where geothermal resources are thought to be located in the Karckar region (Fig. 3). Gravity data were collected to: (i) identify geological discontinuities associated with potential fault-bounded basins; and (ii) provide data to constrain basin depth, a key parameter for understanding the circulation and heating of groundwater. The primary origin of gravity anomalies in the area is related to the density contrast between quartz monzonite identified in an existing borehole, Borehole 4 (Georisk, 2008) (Fig. 3), and the volcanoclastic and alluvial package that fills the fault-bounded basin mapped within the survey area.

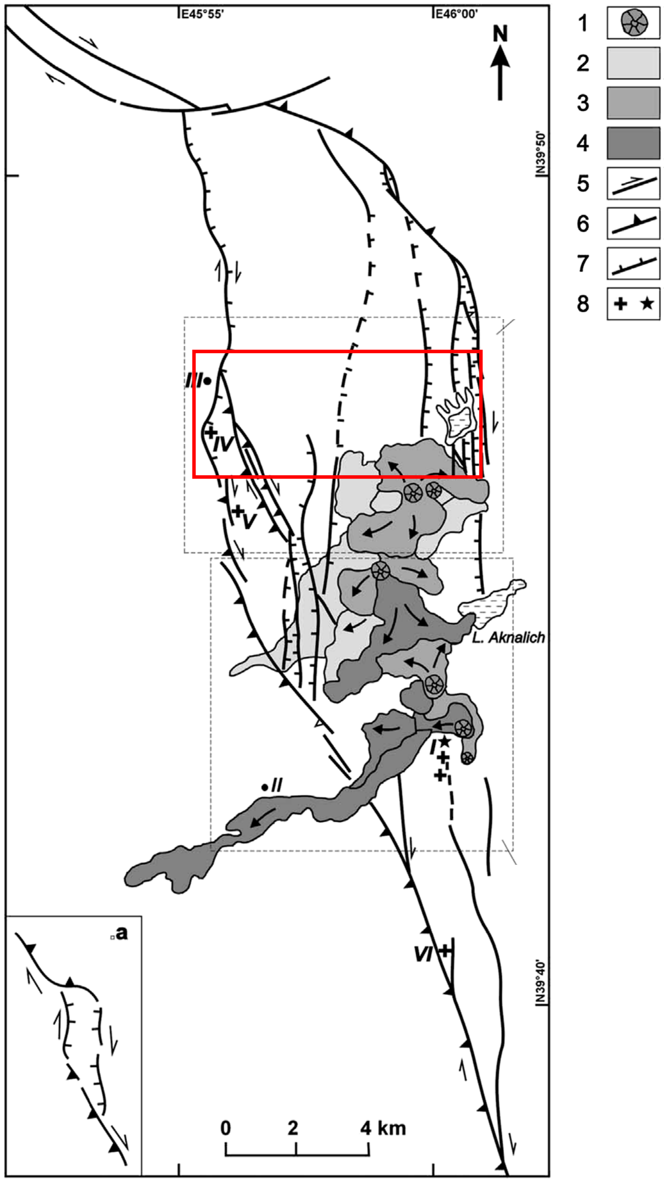

Fig. 2. Geologic map of the Karckar volcanic field and study area. 1, Volcanoes; 2, generation 1 Holocene lava; 3, generation 2 lava; 4, generation 3 Holocene lavas; 5, strike-slip faults; 6, reverse faults; 7, normal faults; 8, petroglyph fields and ancient structures. (a) Conceptual geodynamic model of the Sunik pull-apart basin. Red box marks the approximate extent of study area (dashed boxes and roman numerals are not relevant to this study). Reproduced with permission from Karakhanian et al. (2002). (For interpretation of the references to color in this figure legend, the reader is referred to the web version of this article.)

3.1. Data collection and processing

A total of 257 gravity stations were occupied on a nearly uniform grid over a 40 km^2 area bounded by 578,793 m west, 587,175 m east, 4,402,948 m south, and 4,407,061 m north (WGS84, UTM zone 38 N). Gravity data were digitally acquired using two Scintrex (Scintrex Ltd., Ontario, Canada) CG-5 gravimeters and downloaded daily. Differential GPS positions were recorded at each station using a Trimble 7 data acquisition system. This system included an R7 base GPS receiver and two R7 rover GPS receivers with internal UHF radio modems. The GPS receivers used Trimble (Trimble Navigation Ltd., Sunnyvale, CA) Zephyr Mod-2 GPS antennas which have a carrier phase measurement accuracy to less than 1 mm in a 1 Hz bandwidth. Realtime kinematic surveying gives 10 mm horizontal accuracy and 20 mm vertical accuracy. Using the OSU91A geoid model the WGS84 coordinates obtained from the GPS system were transformed to local orthometric heights. As a check, 36 stations were re-surveyed with a resulting standard deviation in elevation of 0.01 m, corresponding to an error of approximately 0.003 mgal.

The Scintrex CG-5 gravimeter calculates an earth tide correction at each station, based on the date and time of a reading and using coordinates at the center of the survey grid. Instrument drift rate was established before the survey using an overnight drift test after a 48 h instrument warm-up. The CG-5M instrumentation provides a software compensation of drift based on a user-entered estimate of the drift rate based on this drift test.

Gravity teams referenced gravity measurements to a 3-station fixed gravity base network within the survey area (RTK GPS determined base station coordinates). Base network set-up and computations were done 2 days prior to occupying the 257 survey locations. Measurements at these base stations were performed approximately every 4 h during survey days. At least 5 gravity readings were taken at each station, checking for agreement within 0.005 mgal. Data were corrected for residual (linear) drift through the base station tie, and reduced relative to the base station value.

Precise measurements of topography around each station were made and inner and outer terrain corrections were applied. During gravity data acquisition, the operator estimated local terrain with the aid of a Suunto clinometer (Suunto Vantaa, Finland), measuring slope angle around a gravity station within two zones (0 m to 49.9 m and 50 m to 90 m), each zone was subdivided into four quadrants, resulting in 8 topographic measurements per gravity station. The outer correction was applied using an SRTM 90 m DEM (CGIAR, 2008) using a radius from 90 to 10,000 m. Terrain corrections were applied using the WinGLink software (Schlumberger Corp, Houston, TX) a program to process, interpret and integrate gravity data.

Gravity reductions were performed to enhance the local scale of anomalies associated with basement faulting. Briefly, we use the Somigliana closed-form solution (Somigliana, 1930) to estimate theoretical gravity:

$$g_T = \frac{g_e\left(1 + k\sin^2\phi\right)}{\left(1 - e^2\sin^2\phi\right)^{\frac{1}{2}}}, \tag{1}$$

where g_T, is the theoretical gravity on the GRS80 (http://earth-info.nga.mil/GandG/wgs84/) reference ellipsoid at latitude ϕ, g_e is normal gravity at the equator equal to 978,032.67715 mgal, k is a dimensionless derived constant equal to 0.001931851353, and e is the first numerical eccentricity with e^2 having a value of 0.0066943800229. For the GRS80 ellipsoid the second-order formula for the precise free air correction is:

$$\delta g_h = -\left(0.3087691 - 0.0004398\sin^2\phi\right)h + 7.2125 \times 10^{-8}h^2, \tag{2}$$

where the free air correction, δg_h, is calculated in milligals and h is the elliptical elevation of the gravity station measured in meters.

The weight of the atmosphere varies with height and this change affects gravity measurements. The atmospheric correction accounts for the change in weight of the atmosphere between the base station and the measurement point. The formula for the atmospheric correction is:

$$\delta g_{atm} = 0.874 - 9.9 \times 10^{-5}h + 3.56 \times 10^{-9}h^2, \tag{3}$$

where the atmospheric correction, δg_{atm}, is given in milligals and h is the elliptical elevation of the gravity station in meters.

The Bouguer correction accounts for the mass of average crustal rock between the base station and the measurement point, given the height difference between them. The Bouguer correction used here accounts

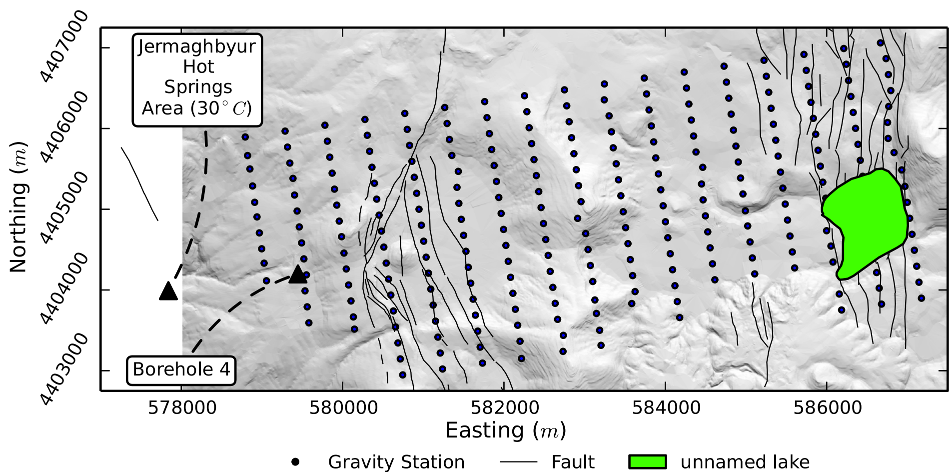

Fig. 3. Study area.

for the spherical cap-shape of this mass of rock, as described in LaFehr (1991):

$$g_{sc} = 2\pi G\rho[(1+\mu)h - \lambda R], \tag{4}$$

where g_{sc} is the gravity correction in milligals resulting from the spherical cap, ρ is the density of the material making up the spherical cap in kg m^{-3}, μ and λ are dimensionless coefficients, and $R = R_0 + h$, where R_0 is the mean radius of the Earth in meters and h is the elevation of the gravity station on the reference ellipsoid in meters. A terrain correction was applied using a digital elevation model and terrain estimates near the gravity station with an assumed density of 2550 kg m^{-3} (Kane, 1962; Campbell, 1980; Blais and Ferland, 1984; Nowell, 1999); for all gravity stations, the terrain correction was <1 mgal.

Because we are most interested in the local variation in the gravity field (i.e., within the boundaries of the survey area), a residual gravity anomaly was computed by subtracting the complete Bouguer anomaly (the anomaly obtained after the application of the terrain correction) from an assumed regional trend, estimated by fitting a plane to the complete Bouguer anomaly map using the generalized least-squared method (Aster et al., 2013).

Recalculation of the gravity map using a range of Bouguer densities showed that correlation with local topography is minimized using a specific range of densities, 2300 kg m^{-3} $\leq \rho \leq$ 2550 kg m^{-3}. Much of the topography around the site was formed by lava flows. In Hawaii, basalt density measurements in boreholes are 2000–3000 kg m^{-3}, with mean value of 2500 kg m^{-3} for water saturated lava flows (Moore, 2001). Karckar lava flows should be close to this density, or perhaps slightly less for partially saturated rocks that form topographic highs in the local survey area. The observation data selected for inversion is the complete Bouguer gravity anomaly at each gravity station calculated with a Bouguer density of 2550 kg m^{-3} (Fig. 4).

3.2. Gravity model

The forward gravity model consists of 8468 rectangular prisms (Blakely, 1996) aligned in a non-uniform grid that is approximately centered on the dataset of observed gravity stations. Rectangular prisms range from 100 m^2 in the area of the gravity stations to 1500 m^2 distal from the gravity stations. Each prism extends from the surface to some depth, inferred through the inversion. Thus the prisms represent the thickness of a package of alluvium, volcanoclastics, and lava flows overlying the quartz monzonite intrusions and related basement rocks. The depth of each prism is adjusted during the inversion process to minimize differences between the observed gravity field and the calculated gravity field.

For the gravity inversion, the density contrast of each prism was fixed at a value of −375.0 kg m^{-3}, which is assumed to represent the bulk density contrast for the valley-fill sediments, volcanoclastics and low-density lava flows with the underlying quartz monzonite or comparable basement. Using a density for the quartz monzonite of 2800 kg m^{-3} (Daly, 1935) the density contrast of −375.0 kg m^{-3} implies a fill density of 2425 kg m^{-3}.

The Levenburg–Marquardt algorithm (LMA) (Marquardt, 1963), in combination with explicit regularization and reparameterization techniques, was used to invert the gravity data for the bottom depth of each prism in the gravity forward model using the parameter estimation software PEST (Doherty, 2012). The LMA is based on the Gauss–Newton algorithm that is modified to form a trust region between the quadratic-approximated Newton search direction and the gradient descent direction in parameter space. The operating equation of the LMA is

$$\theta_n = \theta_c - \left(\mathbf{J}^T\Sigma_\epsilon^{0.5}\mathbf{J} + \lambda\mathbf{I}\right)^{-1}\mathbf{J}^T\Sigma_\epsilon^{0.5}\mathbf{r}, \tag{5}$$

where $\mathbf{J}$ is the Jacobian matrix evaluated at θ_c, λ is the Marquardt parameter, $\mathbf{I}$ is the identity matrix, Σ_ϵ is the observation covariance matrix, $\mathbf{r}$ is the residual vector, and θ_n and θ_c are the new and current parameter vectors, respectively. The residual vector, $\mathbf{r}$, is calculated as observed data minus the model-simulated equivalents. By increasing the value of λ, the upgrade direction is rotated from the Newton direction to the direction of gradient descent. The residual vector, $\mathbf{r}$ is calculated as observation data minus the model-simulated equivalents. Iterations with Eq. (5) are continued until a minimum of the weighted least-squares objective function is found, which is defined as

$$\phi = (\mathbf{h} - \mathbf{J}\theta)^T\Sigma_\epsilon^{0.5}(\mathrm{h} - \mathbf{J}\theta) \tag{6}$$

where $\mathbf{h}$ is the vector of observations used for inversion and the matrix–vector product $\mathbf{J}\theta$ yields the vector of model-simulated equivalent observations, evaluated at θ.

Pilot points were used as a reparameterization device to reduce the dimensionality of the inverse model, while maintaining the ability of the inverse problem to spatially adjust prism depths to change simulated gravity and match the observed gravity data using the fixed density contrast (Doherty, 2003). The pilot points were distributed non-uniformly throughout the gravity model domain, focused near the gravity stations to provide maximum flexibility to fit the observed gravity anomaly. A total of 554 pilot points were used to parameterize the depth distribution of the forward model grid.

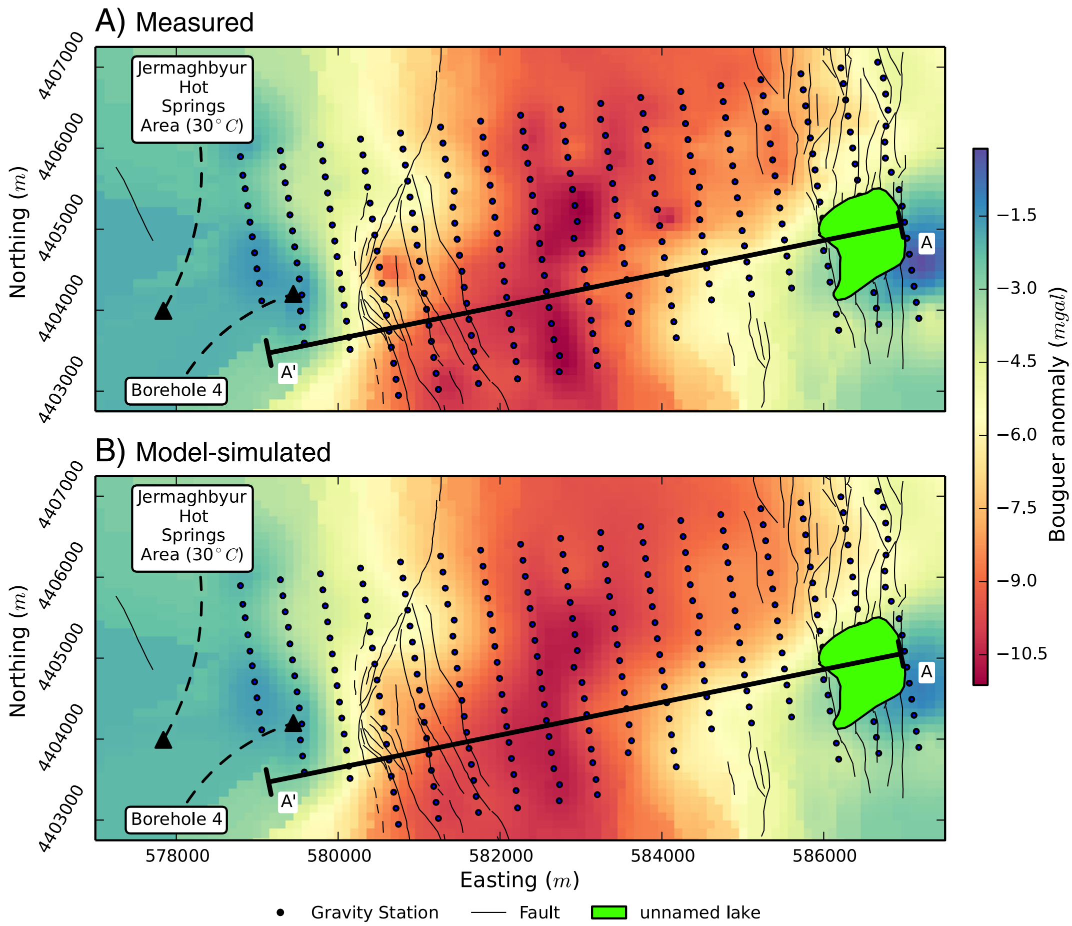

Fig. 4. Comparison of measured and model-simulated Bouguer anomaly. Values were interpolated from gravity stations to model grid; cross section A–A′ marks the location of the hydrothermal modeling domain. (For interpretation of the references to color in this figure legend, the reader is referred to the web version of this article.)

Even with the use of pilot point to reduce the dimensionality of the inverse problem, the number of adjustable parameters (554) outnumbers the number of gravity stations (257). The minimum error variance solution of an ill-posed inverse problem such as this requires finding a pseudo-inverse solution that meets the Moore–Penrose conditions (Koch, 1989). A combination of truncated singular value decomposition (TSVD) regularization (Aster et al., 2013) and Tikhonov regularization (Tikhonov and Arsenin, 1977) was used for the inversion of the basin depth distribution using the 257 processed gravity observations. This approach to gravity inversion results in a pseudo inverse solution that also honors prior knowledge, as implemented with Tikhonov constraints.

TSVD regularization is implemented by applying the singular value decomposition to the quantity $(\mathbf{J}^T\Sigma_\epsilon^{0.5}\mathbf{J}+\lambda\mathbf{I})$ of Eq. (5):

$$\left(\mathbf{J}^T\Sigma_\epsilon^{0.5}\mathbf{J}+\lambda\mathbf{I}\right)=\mathbf{USV}^T, \tag{7}$$

where $\mathbf{U}$ and $\mathbf{V}$ contain the left and right singular vectors, respectively, and $\mathbf{S}$ is a diagonal matrix of decreasing singular values. If p non-zero singular values are along the diagonal of $\mathbf{S}$, then the pseudo inverse is

$$\left(\mathbf{J}^T\Sigma_\epsilon^{0.5}\mathbf{J}+\lambda\mathbf{I}\right)^*=\mathbf{V}_p\mathbf{S}_p^{-1}\mathbf{U}_p^T, \tag{8}$$

where * denotes the pseudo inverse and $_p$ denotes the singular components associated with the first p (non-zero) singular values. Eq. (8) is substituted into (5) to form a stabilized solution to an ill-posed inverse problem.

Tikhonov regularization is implemented by replacing ϕ of Eq. (6) with

$$\phi=\phi_m+\alpha\phi_r=(\mathbf{h}-\mathbf{J}\theta)^T\Sigma_\epsilon^{0.5}(\mathbf{h}-\mathbf{J}\theta)+\alpha\phi_r, \tag{9}$$

where $\mathbf{h}$ is the observation vector, ϕ_m is the weighted least-squares measurement objective function and ϕ_r is the regularization penalty, which represents preferred parameter states. The parameter α controls the enforcement of Tikhonov regularization, where larger values of α results in a poorer fit to observed data but better agreement with preferred parameter states. For the inversion of the basin depth distribution, 1st-order Tikhonov regularization was used to enforce a preferred homogeneity state. See Doherty and Hunt (2010) for more information regarding the implementation of the inversion algorithm.

If a target value of ϕ_m, $\phi_{m_{target}}$, is specified, the inverse problem can be transformed into a constrained optimization problem to maximize α subject to $\phi_m \le \phi_{m_{target}}$. In this framework, the goal of the inversion process is to minimize regularization error constrained by the specified level of assumed measurement noise. We assume a measurement error associated with each gravity station that is normally distributed and uncorrelated with a standard deviation of 0.1 mgal.

The inverted basin depth distribution of the 8468 prisms is shown in Fig. 5 and a comparison of the measured and model-simulated Bouguer anomaly is shown in Fig. 4. Through the use of 1st-order Tikhonov regularization and the specified level of measurement noise, the resulting basin depth distribution is the “smoothest” possible solution that is consistent with the assumed level of measurement noise.

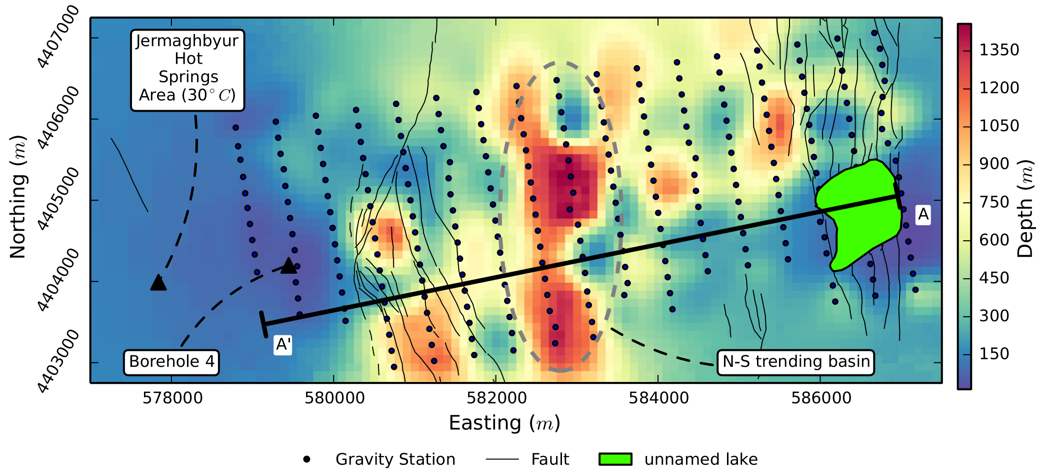

Fig. 5. The location of the cross section (thick black line) used for the development of the 2-D hydrothermal transport model (Fig. 7) is superimposed on the inversion model of the gravity anomaly based on a Bouguer density of 2550 kg m^{-3}. Colors indicate the depth distribution of basin-fill, assuming lavas, alluvium, and volcaniclastics on top with quartz monzonite overlying the basement. The Jemaghbyur hot spring area (30 °C) and Borehole 4 are indicated by black triangles. Area faults are indicated by thin black lines. The N–S trending basin is circled in gray. (For interpretation of the references to color in this figure legend, the reader is referred to the web version of this article.)

The major feature of the depth distribution is the presence of a narrow N–S trending basin through the center of the map area, reaching a maximum depth of approximately 1500 m and bounded by mapped faults.

4. Geothermal model

The inverted basin depth derived from the gravity data places important constraints on the hydrothermal circulation model for the Karckar region, and is consistent with observations made in Borehole 4. Interbedded lavas and alluvium occur in Borehole 4 to a depth of 123 m. Quartz monzonite was logged from 123 m to the bottom of the hole at approximately 1000 m depth. The thickness of alluvium and lava flows derived from the gravity model in the westernmost part of the grid, east of Borehole 4, is approximately 150 m. This indicates that the modeled depths from the 3D inversion of gravity data generally represent the depth to basement, which at least in Borehole 4, is quartz monzonite.

Temperature data collected from Borehole 4 show a major temperature shift near 200 m depth (Fig. 6), which we interpret to be an advection-dominated geothermal fluid transport pathway associated with the contact between the quartz monzonite and the overlying lava flows and alluvium. Conceptually, this pathway is thought to be a high-permeability flow zone that may deliver deeply circulating meteoric water to a potential high-enthalpy heat source at depth in the basin, and facilitate surface discharge at Jermaghbyur hot springs

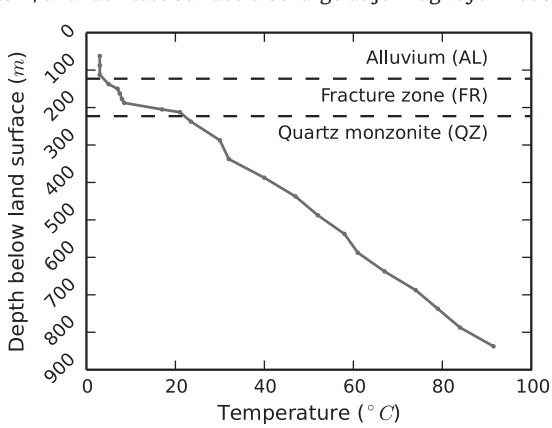

Fig. 6. Measured temperature distribution at Borehole 4.

area, located west of Borehole 4 (Fig. 5), which has a temperature of about 30 °C, similar to the temperature measured near 250 m depth at Borehole 4. Unfortunately, little more is known about the physical and chemical characteristics of the discharge at Jermaghbyur hot springs.

Below approximately 250 m depth, the geothermal gradient measured in Borehole 4 is anomalous, reaching approximately 0.1$\frac{°C}{m}$ in the lower half of the well (Fig. 6). This gradient indicates that an appreciable quantity of heat may be entering the geothermal system as a diffuse heat flux through the insulating quartz monzonite unit. A strong geothermal gradient in the basin also indicates that circulating groundwater may also be exposed to a diffuse heat source that heats deeply circulating groundwater.

Obviously, a heat source at depth is required to explain the anomalous geothermal gradient in Borehole 4, as well as the presence of the down-gradient Jermaghbyur hot springs. However, the nature of the heat source is uncertain. As such, three possible configurations are considered: 1.) a relatively high-enthalpy heat source localized within the fault-bounded basin, for example resulting from a shallow intrusion within or bordering the basin, 2.) a larger, regional, low-enthalpy diffuse heat source resulting from thinning of the crust and distributed magmatism or 3.) a combination of high-enthalpy local and low-enthalpy regional heat sources.

4.1. Hydrothermal model framework

A density-dependent groundwater flow and transport model was constructed to simulate advective and conductive heat transport for the Karckar geothermal system and evaluate the potential for a high-enthalpy localized heat source (if any) at depth within the pull-apart basin. This model is based on results from the gravity inversion and was parameterized using site-specific data and expected values from literature sources. Results from the model were compared to the measured temperature distribution in Borehole 4 (Fig. 6) to evaluate the reasonableness of different geothermal source configurations.

A two-dimensional cross-section hydrothermal model domain was used for this analysis. The hydrothermal model domain extends along an inferred groundwater flow path parallel to the long axis of the gravity grid through the unnamed lake (a recharge feature) in the eastern part of the study area and just south of Borehole 4 in the west (Fig. 5). This hydrothermal model domain was selected because it is thought to be representative of the general geothermal circulation pattern across the basin and allows inclusion of the prominent flow system features.

Furthermore, the selected hydrothermal model domain is approximately normal to the strike of the pull-apart basin. Conceptually, water enters the model domain either as a flux from the unnamed lake or as meteoric recharge applied to the top model layer and is discharged as either evapotranspiration out of the top model layer or through the western, down-gradient boundary.

Based on the gravity inversion and the lithologic log from Borehole 4, the subsurface along the cross-section was simplified into three distinct geologic units: (*i*) alluvium and lava flows (AL), (*ii*) Upper quartz monzonite that is interpreted to be highly fractured (FR), and (*iii*) lower quartz monzonite that is less fractured (QZ).

These units were translated into three separate hydrostratigraphic units for input into the hydrothermal model as regions of distinct hydraulic and transport model parameters. The basin depth, as determined from the gravity inversion, represents the contact between the AL and FR units (Fig. 7). Based on the lithologic record from Borehole 4, the FR unit is conceptualized as having a uniform thickness of 100 m, so that contact between the FR and QZ units is 100 m below the contact between the AL and FR units. The AL unit comprises the lower density alluvium and lava flows that fill the valley, as interpreted from the gravity inversion. The FR unit is thought to be a primary transport pathway for advective heat transport from the deep part of the basin to shallower depths near Borehole 4.

The groundwater modeling code SEAWAT Version 4 (Langevin et al., 2008) in conjunction with FLOPY (Bakker et al., 2013) was used as the simulation engine for the hydrothermal model analysis. SEAWAT Version 4 solves a density-dependent form of the groundwater flow equation and is capable of multi-species density-dependent transport. SEAWAT Version 4 uses a finite-difference approximation and is capable of simulating the transport of heat by both conductive and advective processes:

$$\nabla \cdot \left[\rho \frac{\mu_0}{\mu} \mathbf{K}_0 \left(\nabla h_0 + \frac{\rho - \rho_0}{\rho_0} \nabla z\right)\right] = \rho S_{s,0} \frac{\partial h_0}{\partial t} + \theta \frac{\partial \rho}{\partial C} \frac{\partial C}{\partial t} - \rho_s q_s', \tag{10}$$

where ρ_0 is fluid density at reference conditions in kg m^{-3}, μ is dynamic viscosity in kg m^{-1} s^{-1}, μ_0 is dynamic viscosity at reference conditions in kg m^{-1} s^{-1}, $\mathbf{K}_0$ is hydraulic conductivity tensor at reference conditions in ms^{-1}, h_0 is hydraulic head at reference conditions in meters, $S_{s,0}$ is specific storage in m^{-1}, t is time in s, θ is porosity in m^3 m^{-3}, C is concentration in kg kg^{-1}, and q_s' is source/sink term of fluid with density ρ_s in kg s^{-1} m^{-3}. The SEAWAT Version 4 user's manual (Langevin et al., 2008) as well as Langevin et al. (2010) and Thorne et al. (2006) provide a complete derivation, implementation details, and results from several benchmark problems. See Hughes et al. (2010) for an application of SEAWAT Version 4 in a heat transport setting.

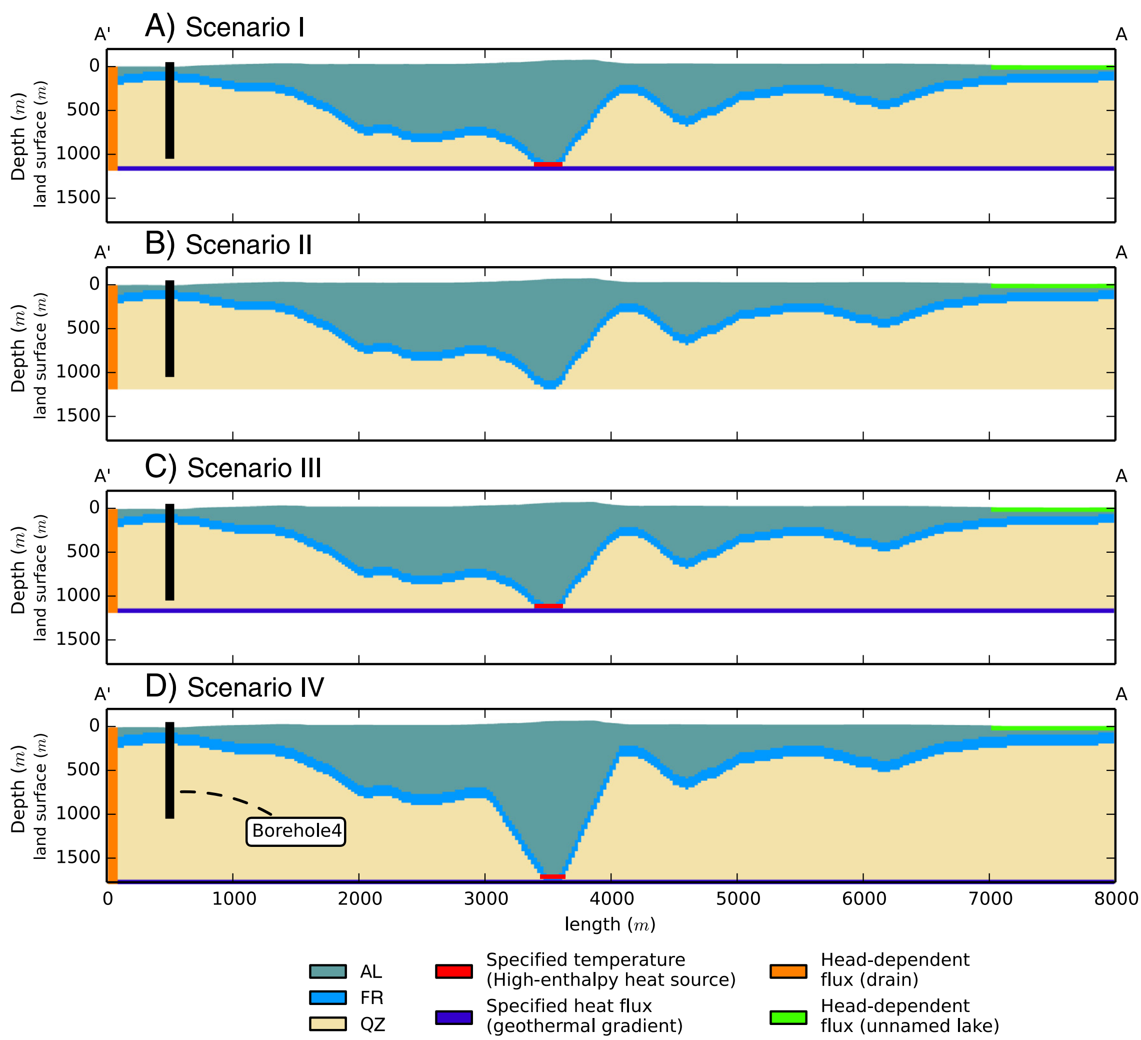

Fig. 7. Model scenarios that evaluate potential geothermal system configurations. The location of cross section A–A′ is shown on Fig. 5. A.) Scenario I includes only a specified heat flux boundary condition. B.) Scenario II includes only a specified temperature boundary condition. C.) Scenario III includes both a specified temperature boundary condition at the deepest part of the basin and a specified heat flux boundary condition across the bottom of the model domain. D.) Scenario IV includes both types of heat source boundary conditions, but the deepest part of the basin was lowered to evaluate the effect of possible gravity inversion biases. (For interpretation of the references to color in this figure legend, the reader is referred to the web version of this article.)

To simulate heat transport in SEAWAT, heat is treated as a dissolved constituent. As a result, the SEAWAT framework requires specification of thermal properties, including fluid-matrix thermal distribution coefficient ($K_{d_{temp}}$), effective molecular diffusion coefficient for heat transport ($D_{m_{temp}}$), and viscosity dependence on temperature ($\mu(T)$).

The thermal distribution coefficient, K_{d_temp}, describes thermal equilibrium between the aquifer and the fluid:

$$K_{d_temp} = \frac{c_{Psolid}}{\rho c_{Pfluid}}, \tag{11}$$

where c_{Psolid} is the specific heat capacity of the aquifer material in $m^2\ s^{-1}\ °C^{-1}$ and c_{Pfluid} is specific heat capacity of the fluid in $m^2\ s^{-1}\ °C^{-1}$.

The effective molecular diffusion coefficient describes the transport of heat by matrix and fluid conduction:

$$D_{m_temp} = \frac{k_{Tbulk}}{\theta \rho c_{Pfluid}}, \tag{12}$$

where k_{Tbulk} is bulk thermal conductivity in kg $m^3\ s^{-2}\ °C^{-1}$.

Bulk thermal conductivity, k_{Tbulk}, is calculated as the arithmetic mean of fluid and aquifer material thermal conductivity:

$$k_{Tbulk} = \theta k_{Tfluid} + (1-\theta) k_{Tsolid} \tag{13}$$

where k_{Tfluid} is fluid thermal conductivity in W $m^{-1}\ °C^{-1}$, and k_{Tsolid} is aquifer material thermal conductivity in W $m^{-1}\ °C^{-1}$.

The dependence of viscosity on temperature is expressed as the ratio, μ_0/μ (Eq. (10)), which affects the hydraulic conductivity tensor. This dependence is implemented with:

$$\mu(T) = 239.4 \times 10^{-7} 10^{\frac{248.37}{T+133.15}} \tag{14}$$

where $\mu(T)$ is viscosity as a function of temperature in kg $m^{-1}\ s^{-1}$ and T is the temperature of the fluid in °C. SEAWAT does not simulate multiphase transport, so the practical upper limit of temperature is 99.0 °C (Langevin et al., 2008).

The use of the finite-difference approximation requires discretization of the continuous partial differential equation into a discrete form for numerical solution. In this case, the discretization includes both spatial discretization, which divides the model domain into cells, or nodes, as well as temporal discretization into discrete solution time steps. The cross-section model was discretized into cells, 25 m square, which results in 48 model layers and 320 model columns. Fig. 7 shows the discretized hydrostratigraphic layers for different modeling scenarios (discussed in Section 4.2). Note that each of the three hydrostratigraphic units is represented by multiple model layers to provide vertical resolution for the heat transport process.

The time-stepping scheme in the model is variable. Groundwater flow time steps increased from a minimum length of 14 min to a maximum time step length of 10 days using a geometric progression and a power of 1.1. Transport time steps were dynamically determined to ensure that the Courant–Friedrichs–Lewy stability condition number (Lewy and F.K.C.R., 1928) of 1.0 was satisfied.

Solution of the partial differential equations for groundwater flow and heat transport requires specification of boundary conditions that represent sources and sinks of water and heat. Flow boundary conditions include:

(1) the unnamed lake near the eastern edge of the model domain was specified as a head-dependent (Cauchy) boundary condition;
(2) outflow at the western (downgradient) edge of the model domain was specified as a head-dependent flux (Cauchy) drain-type boundary condition;
(3) recharge was represented as a specified flux (Neumann) boundary condition; and
(4) evapotranspiration was specified as a head-dependent (Cauchy) boundary condition.

Specified groundwater flow boundary condition values are summarized in Table 1. Note that the western boundary condition was specified as a drain-type boundary because it functions only as a sink for both groundwater and heat.

Heat-transport boundary conditions include:

(1) geothermal heat flux into the basal model layer, represented as a specified flux (Neumann) boundary condition;
(2) a localized heat source in the bottom of the basin as a specified temperature (Dirichlet) boundary condition;
(3) heat transported into the model domain by lake leakage as a specified temperature (Dirichlet) boundary condition;
(4) heat transported into the model domain by recharge as a specified temperature (Dirichlet) boundary condition;
(5) heat transported out of the model domain by evapotranspiration as a specified temperature (Dirichlet) boundary condition; and
(6) heat transported out of the model domain by the head-dependent flux (Cauchy) drain-type boundary at the western (downgradient) edge of the model domain.

Specified heat transport boundary condition values are summarized in Table 2.

The geothermal gradient observed at Borehole 4 and the thermal conductivity, k_{dtemp}, of the basal model layer were used to calculate the basal geothermal heat flux. A temperature of 99.0 °C was selected for the potential high-enthalpy heat source cells, which were placed in model cells where the contact between the AL and FR units is deeper than 1000.0 m (Fig. 7 A, C, D).

The model requires specification of several hydraulic properties for each of the three hydrostratigraphic units including hydraulic conductivity, hydraulic storage, and porosity. Specific yield was also specified for each layer because the groundwater flow system is unconfined. The values assigned to these properties represent expected values from literature sources (Freeze and Cherry, 1979) (Table 3). Note that hydraulic storage properties, while required as model inputs, are not important to the model results because the flow boundary conditions are constant with respect to time.

In addition to the hydraulic properties, transport-specific parameters were also specified for each of the three units, and include specific heat capacity, density, and thermal conductivity. The values assigned to these properties represent expected values from literature sources (Langevin et al., 2008), with the exception of the density of the AL unit which was specified to have the same value used in the Bouguer gravity reduction (Table 4).

4.2. Model scenarios

Model scenarios were constructed to evaluate distinct geothermal source configurations as well as evaluate the sensitivity of assumptions made for the gravity inversion. Comparing the scenario results to the temperature distribution measured at Borehole 4 allows us to constrain

Table 1
Summary of specified flow boundary condition components.

Boundary condition component	Units	Value	Source
Lake stage	m	42.0	DEM
Lake-bed hydraulic conductance	m^2/d	Variable	Calculated using K
Stage at western head-dependent flux drain-type boundary	m	0.786	DEM
Conductance at western boundary	m^2/d	variable	Calculated using K
Recharge rate	m/yr	0.075	10% of annual precip
Maximum evapotranspiration rate	m/yr	0.0675	90% of recharge

Table 2
Summary of specified transport boundary condition components.

Boundary condition component	Units	Value	Source
Geothermal heat flux	W/m^2	0.35	Calculated
Localized heat source	°C	99.0	Geothermal gradient
Transport by lake leakage	°C	1.0	Borehole 4 log
Transport by recharge	°C	1.0	Borehole 4 log
Transport by evapotranspiration	°C	1.0	Borehole 4 log

the enthalpy classification of the system as well as evaluate the importance of simplifying assumptions.

Scenario I simulates a high-enthalpy heat source thermally coupled to the FR and AL units without a regional diffuse heat source. This scenario was constructed by placing a specified temperature boundary condition at the deepest part of the basin and removing the geothermal heat flux cells in the basal model layer (Fig. 7 A).

Scenario II simulates a high-enthalpy heat source thermally insulated from the FR and Al units. Scenario II was constructed by removing the specified temperature cells at the deepest part of the basin and specifying a geothermal heat flux across basal model layer that corresponds to a geothermal gradient of 0.15 °C/m. This thermal boundary configuration represents a diffuse high-enthalpy source that is thermally insulated from the FR and AL units (Fig. 7 B).

Scenario III simulates a combined localized high-enthalpy heat source that is thermally coupled to the FR and AL units as well as a regional diffuse heat source. This scenario was constructed by placing a specified temperature boundary condition at the deepest part of the basin and specifying a geothermal heat flux across basal model layer that corresponds to geothermal gradient of 0.10 °C/m (Fig. 7 C).

Scenario IV tests some assumptions made in the gravity inversion. Specifically, we evaluate the combined effects of an assumed depth-independent density used for the AL unit in the gravity forward and the assumed gravity station standard deviation of 0.1 mgal. These two assumptions may combine to result in a deeper basin depth than was indicated by inversion. We evaluate the sensitivity of the hydrothermal modeling results to these assumptions by modifying the model inputs used in Scenario III. For Scenario IV, the number of model layers is increased from 48 to 72 and the deepest basin depth along the hydrothermal model cross-section was lowered from about 1200 m to about 1800 m (Fig. 7 D). Similar to Scenario III, a high-enthalpy source was simulated by placing specified temperature boundary conditions at the deepest part of the basin and a geothermal heat flux of 0.10 °C/m was specified for model layer 72.

Flow and transport boundary conditions were not modified during the simulation period (steady-state boundary conditions). Each model scenario was run forward in time until the simulated water level and heat distributions were in equilibrium with specified boundary conditions.

Additional simulations were constructed to evaluate the importance of the highly-transmissive FR unit because the capacity of the FR unit to serve as a heat transport pathway across the entire domain is uncertain. This assumption was tested by running Scenarios I, II and III with two hydrothermal parameterizations: *homogeneous*: the hydraulic and thermal properties of the FR and AL units are the same and *heterogeneous*: the hydraulic and thermal properties of the FR and AL units are different, as specified in Tables 3 and 4.

Table 3
Summary of flow model parameters.

Property	Units	AL	FR	QZ
Hydraulic conductivity	m/d	10.0	10.0 to 100.0	0.0001
Porosity	(none)	0.1	0.2	0.08
Specific yield	(none)	0.08	0.12	0.0001
Specific storage	1/m	0.0001	0.0001	0.0001

Table 4
Summary of transport model parameters.

Property	Units	AL	FR	QZ
Density	kg/m^3	2550	2700	2770
Specific heat	J/(kg °C)	840.0	820.0	790.0
Thermal conductivity	W/(m °C)	1.75	1.0	3.0

Simulation results were compared to the measured temperature distribution at Borehole 4 to determine reasonableness. If the model-simulated distribution captures the general shape and trend of the measured distribution, then the scenario is deemed reasonable and the possibility of its existence cannot be rejected.

4.3. Model results

Scenario I was completed to test the existence of an isolated high-enthalpy heat source that is thermally coupled to the FR and AL units by placing 99 °C specified temperature cells at the deepest part of the basin (Fig. 7). Results from both parameterizations indicate this scenario is not reasonable (Fig. 9), as the simulated temperature distribution at Borehole 4 does not generally agree with the measured temperature distribution. For the heterogeneous case, the model simulates a near isothermal temperature distribution at Borehole 4, which is a result of large quantities of heat being advectively transported down gradient from the specified temperature cells within the FR unit (Fig. 8 A). While the homogeneous case is less extreme, it is still not in general agreement with the measured temperature distribution.

Scenario II, which represents a diffuse geothermal source, is reasonable from both parameterizations (Fig. 9). Note the good agreement between the simulated and measured temperature distribution for both the homogeneous and heterogeneous case. In this scenario, groundwater infiltrates near the lake and as recharge, gradually warms along deep-circulation flow paths within the FR and AL units, and discharges near the Jermaghbyur hot springs (Fig. 8 B).

Scenario III evaluates the possibility of a combined high-enthalpy heat source and diffuse, regional heat source contributing energy to the Karckar geothermal system. Comparing the measured temperature data from Borehole 4 to the model-simulated equivalents shows that this scenario is not reasonable (Fig. 9). The homogeneous case better reproduces the temperature measured at Borehole 4 than the heterogeneous case. However, even the homogeneous parameterization over-predicts groundwater temperatures near the surface (Fig. 8 B).

Scenario IV evaluates the sensitivity of the model-predicted temperature distribution at Borehole 4 to the assumptions made for the gravity inversion. Results from both parameterizations reveal a simulated temperature distribution at Borehole 4 that does not agree with the measured distribution (Fig. 9). These results indicate that the hydrothermal modeling results are not likely to be biased by the assumed depth-independent AL unit density or the assumed gravity station error model.

Given the scenario results, the most likely explanation of the temperature distribution from Borehole 4 is a cooling quartz monzonite body (or deeper feature) that is thermally insulated from the highly-transmissive FR and AL units. The apparent likelihood of a diffuse heat source, represented in the model as an increased heat flux across the basal model layer, indicates that the geothermal source can most likely be classified as a low-enthalpy, liquid dominated system. In all cases, the specification of a 99 °C boundary condition, which is generally the upper limit of the “low-enthalpy” classification (Williams et al., 2011), results in too much heat input into the system.

5. Discussion

The coupling of high-resolution gravity inversion with hydrothermal modeling provides a robust and computationally feasible framework to

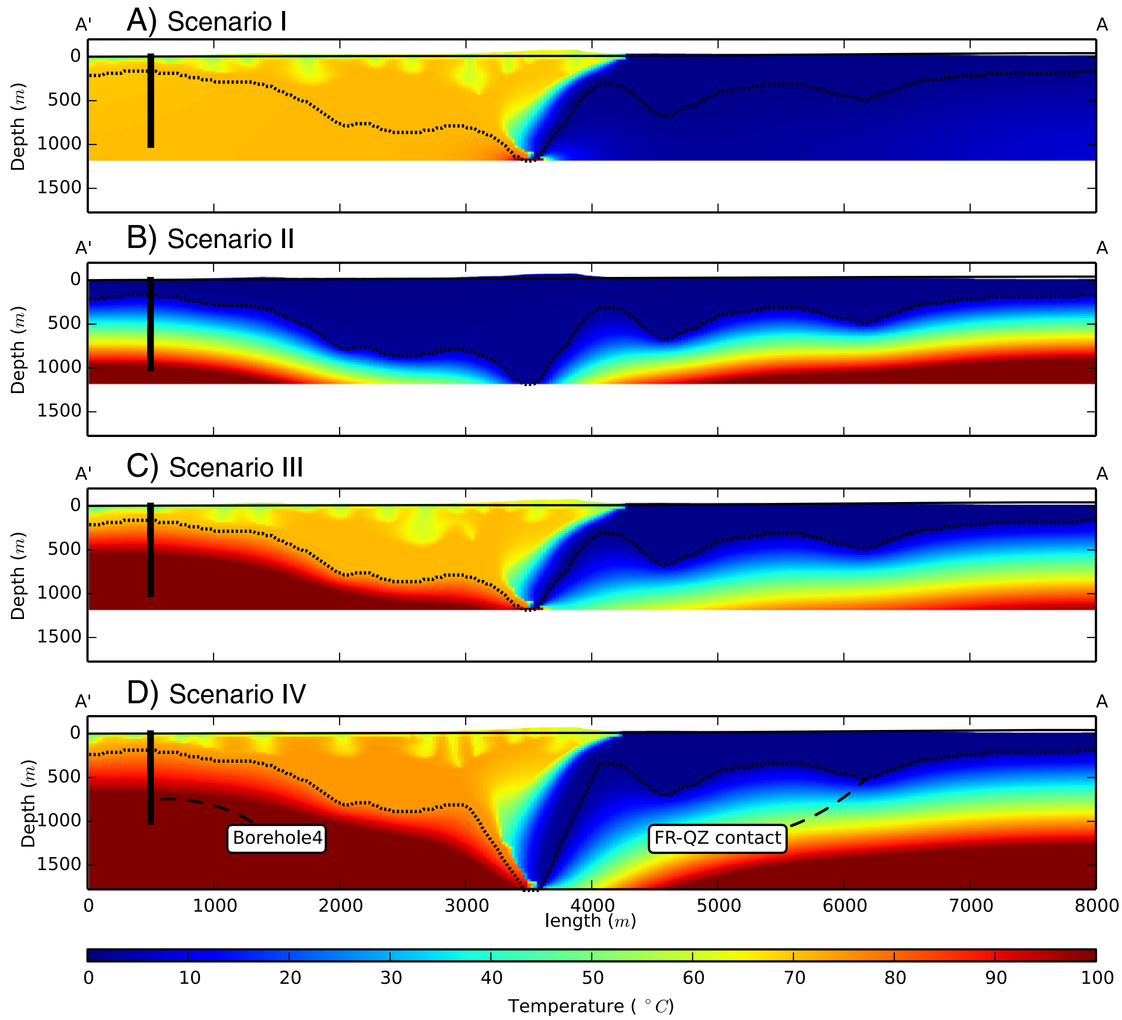

Fig. 8. Comparison of the temperature distribution within the active model domain for the heterogeneous parameterization for Scenario I (localized high enthalpy source at the base of pull-apart basin), Scenario II (distributed geothermal gradient) and Scenario III (combined localized and distributed heat sources) and Scenario IV (Scenario III with increased basin depth). (For interpretation of the references to color in this figure legend, the reader is referred to the web version of this article.)

evaluate potential geothermal resources. The gravity inversion yields an inverted basin depth distribution that is consistent with the prior geologic model of the area and also fits the gravity station data to the level of the associated error model. The use of the inverted basin depth in the hydrothermal model provides key information that facilitates evaluation of several geothermal system configurations that are consistent with and constrained by the geology of the area.

The hydrothermal modeling appears to rule out the *requirement* of a high-enthalpy heat source at depth in the basin. Of the alternative models tested, a diffuse heat source resulting in elevated geothermal

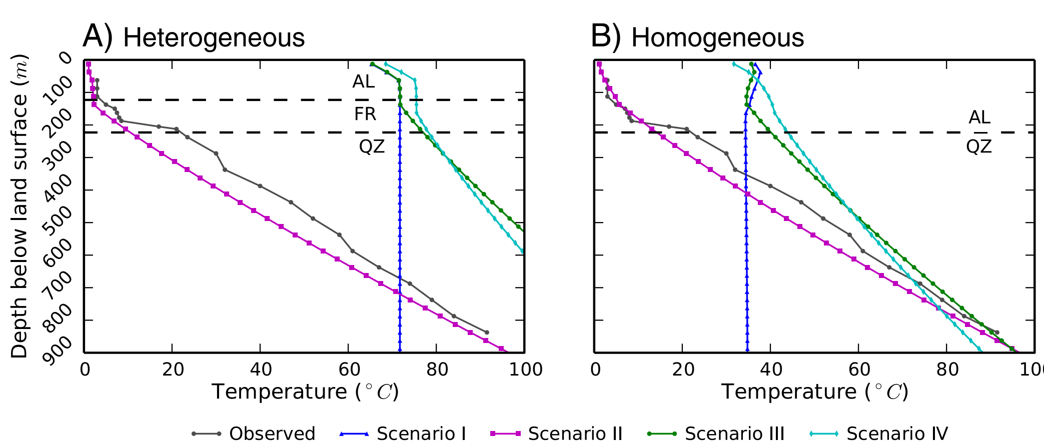

Fig. 9. Comparison of the measured and simulated temperature distribution at Borehole 4 for Scenario I (localized high enthalpy source at the base of pull-apart basin), Scenario II (distributed geothermal gradient), Scenario III (combined localized and distributed heat sources) and Scenario IV (Scenario III with increased basin depth). Scenario II is the most reasonable for the homogeneous and heterogeneous parameterizations.

gradient appears to best explain the temperature data collected from Borehole 4 and its relationship to the quartz monzonite and the basin. In this model, fluids do circulate in the basin, but the dominant heat input into the system is associated with conductive cooling of the quartz monzonite body or a deeper feature that is thermally insulated and advectively isolated from major transmission pathways.

Given the current (2015) state of knowledge about the Karckar geothermal system, a non-identifiability exists between the location and temperature of the postulated heat source within the QZ unit. The hydraulic properties of the QZ unit restrict advective transport while the QZ unit also functions as a thermal insulator, restricting the transport of heat by conduction. The result is a weak thermal coupling between a potential high-enthalpy heat source within the QZ and the advection dominant FR. Therefore, the existence of and depth to a high-enthalpy heat source within the QR unit cannot be determined with any certainty. However, the competence of the QZ unit, as characterized by the data from Borehole 4, indicates that a potential high-enthalpy source within the QZ unit may have very little geothermal fluid with which to interact.

A series of simulations were completed to evaluate the sensitivity of geophysical and hydrothermal modeling assumptions and these analyses indicate that conclusions based on the hydrothermal modeling results are not likely to be biased by the parameterization selected for the advective part of the model domain or assumptions used in the gravity inversion. However, not all assumptions made in the analysis can be evaluated and remaining assumptions may create bias. For example, isolated low permeability zones may occur within the AL unit, which was modeled as a homogeneous, relatively-high permeability unit. If so, then a high-enthalpy heat source within the basin may still be present at depth, but may be advectively isolated by a low permeability cap-rock. However, there is no evidence from the geophysical data, borehole data, or models to indicate that the assumption of a homogeneous AL unit is inappropriate. Further, additional hydrothermal simulations were completed that specified a value of 1.0 m/d for hydraulic conductivity of the AL unit. These simulations (not shown) result in unrealistically high water levels across the model domain indicating that if lower permeability zones do exists within the AL unit, these zones are not likely to restrict the circulation of geothermal fluid over large regions.

Any model of a complex hydrothermal circulation system is necessarily a simplification. The simplification needed to build the numerical model may create bias in the interpreted geothermal system enthalpy constraint. However, for the purposes of evaluating the potential existence of a high-enthalpy system within the fault-bounded basin, the hydrothermal modeling analysis has demonstrated that a low-enthalpy geothermal system is reasonable. We note the remarkable agreement between the simulated and measured temperature data using a relatively simple, maximum a priori hydraulic and thermal properties, which gives additional confidence in the hydrothermal modeling results. Additionally, hydraulic and thermal property heterogeneities obviously exist in the subsurface in the study area and, given the lack of data to constrain the modeling, numerous combinations of subsurface properties and geothermal source configurations will likely fit the Borehole 4 temperature data. However, using uniform subsurface property values, we are able to demonstrate that a low-enthalpy geothermal source cannot be disproved given state of knowledge about the study area, which is an important result for the potential development of this geothermal resource.

Note that the modeling scenarios constructed for this study were specifically designed to evaluate the geothermal system in the Karckar area. As such, these modeling scenarios are not suitable for any other use.

6. Conclusions

Geophysical data collection and inversion were used to provide key geothermal circulation model inputs and boundary conditions. Specifically, inversion of high-quality gravity station data was used to define the thickness of the alluvium and/or lava flows filling a pull-apart basin. The inverted basin depth was used to define the hydrostratigraphic units for a hydrothermal modeling analysis. The hydraulic and thermal properties in the model were assigned using simple parameterization schemes based on maximum a priori estimates. Four distinct geothermal target configurations consisting of combinations of high-enthalpy and/or low-enthalpy geothermal targets were tested to evaluate the possible enthalpy classifications. The results of the modeling were compared to an observed temperature distribution near the downgradient edge of the active model domain. Given the current (2015) state of knowledge, the presence of a localized high-enthalpy source cannot be ruled out, but is unlikely. Rather, a diffuse heat flux into the basal model layer is more likely, which conceptually represents a thermally insulated heat source below the basin. This diffuse heat flux is likely an indicative of a low-enthalpy geothermal target.

Acknowledgments

The authors would like to gratefully acknowledge the financial support of the Armenia Geothermal Project, which is part of the Armenia Renewable Resources and Energy Efficiency Fund (R2E2). The gravity station data used for the basin depth inversion were collected by WesternGeco, Integrated EM Center of Excellence Geosystem, Schlumberger Italiana SpA, Milan, Italy, during September–October of 2011, for the Armenia Geothermal Project. Also, the authors thank Tom Roper and his team for the assistance in collection of gravity data.

Any use of trade, firm, or product names is for descriptive purposes only and does not imply endorsement by the U.S. Government.

References

Aster, R., Borchers, B., Thurber, C., 2013. Parameter Estimation and Inverse Problems. Academic Press (URL: http://books.google.com/books?id=ES4wWol_WucC).
Bakker, M., Post, V., Hughes, J., Langevin, C., Frances, A., White, J., 2013. Enhanced FloPy scripts for constructing and running MODFLOW-based models. Proceedings of the 2013 MODFLOW and More Conference.
Blais, J.A.R., Ferland, R., 1984. Optimization in gravimetric terrain corrections. Can. J. Earth Sci. 21, 505–570.
Blakely, R.J., 1996. Potential Theory in Gravity and Magnetic Applications. Cambridge University Press.
Campbell, D.L., 1980. Gravity terrain corrections for stations on a uniform slope — a power law approximation. Geophysics 45, 109–112.
CGIAR, 2008. SRTM 90 m digital elevation database version 4.1. http://www.cgiar-csi.org/data/srtm-90m-digital-elevation-database-v4-1.
Copley, A., Jackson, J., 2006. Active tectonics of the Turkish–Iranian Plateau. Tectonics 25. http://dx.doi.org/10.1029/2005TC001906.
Daly, R., 1935. Densities of rocks calculated from their chemical analyses. Proc. Natl. Acad. Sci. 21, 657–663.
Dewey, J., Hempton, M., Kidd, W., Saroglu, F., Sengor, A., 1986. Shortening of continental lithosphere: the neotectonics of Eastern Anatolia — a young collision zone. Geol. Soc. Lond. Spec. Publ. 19, 1–36. http://dx.doi.org/10.1144/GSL.SP.1986.019.01.01 (URL: http://sp.lyellcollection.org/content/19/1/1.abstract, arXiv:http://sp.lyellcollection.org/content/19/1/1.full.pdf+html).
Doherty, J., 2003. Ground water model calibration using pilot points and regularization. Ground Water 41, 170–177. http://dx.doi.org/10.1111/j.1745-6584.2003.tb02580.x.
Doherty, J., 2012. Pest, Model-Independent Parameter Estimation: User Manual (5th Ed., With Slight Additions). (URL: http://www.pesthomepage.org/Downloads.php).
Doherty, J.E., Hunt, R.J., 2010. Approaches to highly parameterized inversion: a guide to using PEST for groundwater-model calibration. Scientific Investigation Report 2010-5169.
Freeze, R., Cherry, J., 1979. Groundwater. Prentice-Hall (URL: http://books.google.com/books?id=feVOAAAAMAAJ).
Georisk, 2008. Independent interpretation of the results of the 3D MT, gravity and CO2 surveys conducted at the karkar site, georisk/r2e2. Worldbank Report.
Gupta, H., Roy, S., 2006. Geothermal Energy: An Alternative Resource for the 21st Century. Elsevier Science (URL: http://books.google.com/books?id=3sOyhcp5eZYC).
Hughes, J.D., Langevin, C.D., Brakefield-Goswami, L., 2010. Effect of hypersaline cooling canals on aquifer salinization. Hydrogeol. J. 18, 25–38. http://dx.doi.org/10.1007/s10040-009-0502-7.
Jennejohn, D., 2009. Research and Development in Geothermal Exploration and Drilling. Geothermal Energy Association.
Kane, M.F., 1962. A comprehensive system of terrain corrections using a digital computer. Geophysics 27, 455–462.

Karakhanian, A.S., Trifonov, V.G., Azizbekian, O.G., Hondkarian, D.G., 1997. Relationship of late quaternary tectonics and volcanism in the Khanarassar active fault zone, the Armenian Upland. Terra Nova 9, 131–134. http://dx.doi.org/10.1046/j.1365-3121.1997.d01-11.x.

Karakhanian, A., Djrbashian, R., Trifonov, V., Philip, H., Arakelian, S., Avagian, A., 2002. Holocene-historical volcanism and active faults as natural risk factors for Armenia and adjacent countries. J. Volcanol. Geotherm. Res. 113, 319–344. http://dx.doi.org/10.1016/S0377-0273(01)00264-5.

Karakhanian, A.S., Trifonov, V.G., Philip, H., Avagyan, A., Hessami, K., Jamali, F., Bayraktutan, M.S., Bagdassarian, H., Arakelian, S., Davtian, V., Adilkhanyan, A., 2004. Active faulting and natural hazards in Armenia, eastern Turkey and northwestern Iran. Tectonophysics 380, 189–219. http://dx.doi.org/10.1016/j.tecto.2003.09.020 (URL: http://www.sciencedirect.com/science/article/pii/S0040195103005079, active Faults of the Eastern Hemisphere).

Koch, K.R., 1989. Parameter Estimation and Hypothesis Testing in Linear Models. Springer, Berlin, New York (URL: http://opac.inria.fr/record=b1095181. this is a translation of the 3rd German edition ParameterschÃƒÂ¤tzung und Hypothesentests in linearen Modellen – T.p. verso).

LaFehr, T.R., 1991. Standardization in gravity reduction. Geophysics 56, 1170–1178.

Langevin, C., Thorne Jr., D.T., Dausman, A., Sukop, M., Guo, W., 2008. SEAWAT version 4: a computer program for simulation of multi-species solute and heat transport: U.S. Geological Survey techniques and methods book 6, chapter a22. U.S. Geological Survey Techniques and Methods Book 6, Chapter A22. U.S. Geological Survey.

Langevin, C.D., Dausman, A.M., Sukop, M.C., 2010. Solute and heat transport model of the Henry and Hilleke laboratory experiment. Ground Water 48, 757–770. http://dx.doi.org/10.1111/j.1745-6584.2009.00596.x.

Lewy, H., F.K.C.R., 1928. Ãœber die partiellen differenzengleichungen der mathematischen physik. Math. Ann. 100, 32–74 (URL: http://eudml.org/doc/159283).

Marquardt, D., 1963. An algorithm for least-squares estimation of nonlinear parameters. J. Soc. Ind. Appl. Math. 11, 431–441. http://dx.doi.org/10.1137/0111030.

Moore, J.G., 2001. Density of basalt core from hilo drill hole, Hawaii. J. Volcanol. Geotherm. Res. 112, 221–230. http://dx.doi.org/10.1016/S0377-0273(01)00242-6 (URL: http://www.sciencedirect.com/science/article/pii/S0377027301002426).

Muffler, L., 1993. Tectonic and hydrologic control of the nature and distribution of geothermal resources. Geo-Heat Center Quarterly Bulletin.

Nowell, D.A.G., 1999. Gravity terrain corrections — an overview. J. Appl. Geophys. 42, 117–134.

Philip, H., Cisternas, A., Gvishiani, A., Gorshkov, A., 1989. The Caucasus: an actual example of the initial stages of continental collision. Tectonophysics 161, 1–21. http://dx.doi.org/10.1016/0040-1951(89)90297-7 (URL: http://www.sciencedirect.com/science/article/pii/0040195189902977).

Philip, H., Rogozhin, E., Cisternas, A., Bousquet, J.C., Borisov, B., Karakhanian, A., 1992. The Armenian earthquake of 1988 December 7: faulting and folding, neotectonics and palaeoseismicity. Geophys. J. Int. 110, 141–158. http://dx.doi.org/10.1111/j.1365-246X.1992.tb00718.x.

Philip, H., Avagyan, A., Karakhanian, A., Ritz, J.F., Rebai, S., 2001. Estimating slip rates and recurrence intervals for strong earthquakes along an intracontinental fault: example of the Pambak–Sevan–Sunik fault (Armenia). Tectonophysics 343, 205–232. http://dx.doi.org/10.1016/S0040-1951(01)00258-X (URL: http://www.sciencedirect.com/science/article/pii/S004019510100258X).

Rebai, S., Philip, H., Dorbath, L., Borissoff, B., Haessler, H., Cisternas, A., 1993. Active tectonics in the lesser Caucasus: coexistence of compressive and extensional structures. Tectonics 12, 1089–1114. http://dx.doi.org/10.1029/93TC00514.

Reed, M., United States Department of Energy, Geological Survey, 1983. Assessment of Low-Temperature Geothermal Resources of the United States—1982. Geological Survey Circular, U.S. Geological Survey (URL: http://books.google.com/books?id=tJOFbwAACAAJ).

Reilinger, R., McClusky, S., Vernant, P., Lawrence, S., Ergintav, S., Cakmak, R., Ozener, H., Kadirov, F., Guliev, I., Stepanyan, R., Nadariya, M., Hahubia, G., Mahmoud, S., Sakr, K., ArRajehi, A., Paradissis, D., Al-Aydrus, A., Prilepin, M., Guseva, T., Evren, E., Dmitrotsa, A., Filikov, S.V., Gomez, F., Al-Ghazzi, R., Karam, G., 2006. GPS constraints on continental deformation in the Africa–Arabia–Eurasia continental collision zone and implications for the dynamics of plate interactions. J. Geophys. Res. Solid Earth 111. http://dx.doi.org/10.1029/2005JB004051.

Rezaie, M., Aghajani, H., 2013. A new combinational terminology for geothermal systems. Int. J. Geosci. 4, 43–48. http://dx.doi.org/10.4236/ijg.2013.41005.

Sanyal, S., 2005. Classification of geothermal systems a possible scheme. Thirtieth Workshop on Geothermal Reservoir Engineering, Stanford University, Stanford, California, pp. 85–88.

Sheriff, R., 1973. Encyclopedic dictionary of exploration geophysics. Society of Exploration Geophysicists (URL: http://books.google.com/books?id=V7G5ngEACAAJ).

Somigliana, C., 1930. Geosica Sul campo gravitazionale esterno del geoide ellissoidico: Atti della Accademia nazionale dei Lincei. Rendiconti. Classe di scienze Ãžsiche. Matematiche e Naturali 6 pp. 237–243.

Thorne, D., Langevin, C.D., Sukop, M.C., 2006. Addition of simultaneous heat and solute transport and variable fluid viscosity to {SEAWAT}. Comput. Geosci. 32, 1758–1768. http://dx.doi.org/10.1016/j.cageo.2006.04.005 (URL: http://www.sciencedirect.com/science/article/pii/S0098300406000768).

Tikhonov, A., Arsenin, V., 1977. Solutions of ill-posed problems. Scripta series in mathematics, Winston. http://books.google.com/books?id=ECrvAAAAMAAJ.

Trifonov, V., Karakhanian, A., Kozhurin, A., 1990. The Spitak earthquake as a manifestation of active tectonics. Geotectonika 6, 46–60.

Trifonov, V., Karakhanian, A., Kozhurin, A., 1994. Major active faults of the collision area between the Arabian and Eurasian plates. Proceedings and Abstracts of the Conference on Continental Collision Zone Earthquakes and Seismic Hazard Reduction.

Williams, C., Reed, M., Anderson, A., 2011. Updating the classification of geothermal resources. Thirty-Sixth Workshop on Geothermal Reservoir Engineering, Stanford University, Stanford, California.

Zaher, M., Saibi, H., Nouby, M.E., Ghamry, E., Ehara, S., 2011. A preliminary regional geothermal assessment of the Gulf of Suez, Egypt. J. Afr. Earth Sci. 60, 117–132.

Zaher, M.A., Saibi, H., Nishijima, J., Fujimitsu, Y., Mesbah, H., Ehara, S., 2012. Exploration and assessment of the geothermal resources in the Hammam Faraun hot spring, Sinai Peninsula, Egypt. J. Asian Earth Sci. 45, 256–267. http://dx.doi.org/10.1016/j.jseaes.2011.11.007 (URL: http://www.sciencedirect.com/science/article/pii/S1367912011004470).